

## Article

# A Novel Dual Self-Centering Friction Damper for Seismic Responses Control of Steel Frame

Juntong Qu <sup>†</sup>, Xinyue Liu <sup>†</sup>, Yuxiang Bai <sup>\*</sup>, Wenbin Wang, Yuheng Li, Junxiang Pu and Chunlei Zhou

School of Architecture and Planning, Yunnan University, Kunming 650504, China; 15808654138@163.com (J.Q.); 18487091835@163.com (X.L.)

<sup>\*</sup> Correspondence: byx@mail.ynu.edu.cn<sup>†</sup> These authors contributed equally to this work.

**Abstract:** Due to their weight, the seismic response control of buildings needs a large-scale damper. To reduce the consumption of shape memory alloys (SMAs), this study proposed a dual self-centering pattern accomplished by the coil springs and SMA, which could drive the energy dissipation device to recenter. Combined with the friction energy dissipation device (FD), the dual self-centering friction damper (D-SCFD) was designed, and the motivation and parameters were described. The mechanical properties of D-SCFD, including the simplified D-SCFD mechanical model, theoretical index calculations of recentering, and energy dissipation performance, were then investigated. The seismic response mitigation of the steel frame adopting the D-SCFDs under consecutive strong earthquakes was finally analyzed. The results showed that a decrease in the consumption of SMA by the dual self-centering pattern was feasible, especially in the case of low demand for the recentering performance. Reducing the D-SCFD's recentering performance hardly affected the steel frame's residual inter-story drift ratios when the residual deformation rate was less than 50%, which can help strengthen the controls on the steel frame's peak seismic responses. It is recommended to utilize the D-SCFD with not too high a recentering performance to mitigate the seismic response of the structure.

**Keywords:** dual self-centering; shape memory alloy; D-SCFD; seismic response mitigation



**Citation:** Qu, J.; Liu, X.; Bai, Y.; Wang, W.; Li, Y.; Pu, J.; Zhou, C. A Novel Dual Self-Centering Friction Damper for Seismic Responses Control of Steel Frame. *Buildings* **2024**, *14*, 407. <https://doi.org/10.3390/buildings14020407>

Academic Editor: Hiroshi Tagawa

Received: 3 January 2024

Revised: 23 January 2024

Accepted: 31 January 2024

Published: 2 February 2024



**Copyright:** © 2024 by the authors. Licensee MDPI, Basel, Switzerland. This article is an open access article distributed under the terms and conditions of the Creative Commons Attribution (CC BY) license (<https://creativecommons.org/licenses/by/4.0/>).

## 1. Introduction

Passive energy dissipation devices can provide additional stiffness and damping for buildings, which improves the safety of buildings by reducing earthquake responses [1,2]. Engineers choose displacement-dependent dampers because of their consistent mechanical performance and inexpensive production costs [3]. Therefore, displacement-dependent dampers have been widely used in the construction and seismic strengthening of buildings located in earthquake-prone areas, such as buckling restrained braces (BRBs), friction energy dissipation devices (FDs), metallic yielding dampers (MYDs), etc. [4–6]. Traditional displacement-dependent dampers, on the other hand, run the risk of causing higher post-earthquake residual deformations of buildings, which can easily raise the economic cost and technological problems of post-earthquake rehabilitation [7]. In this regard, many scholars have developed a series of self-centering dampers to improve the recentering performance of dampers and reduce the post-earthquake residual deformations of buildings [8].

In past research, a kind of self-centering damper simultaneously composed of prestressed tendons and energy dissipation devices has been designed. The prestressed tendons, which mainly include steel strands, basalt fiber tendons, aramid fiber bundles, etc. [9–16]. During the unloading process, the prestressed tendons drive energy dissipation devices to recenter. The self-centering dampers with prestressed tendons often have significant demands for prestressing force to obtain the appropriate recentering effect. However, the demands for high prestressing force will increase the difficulties of manufacturing the dampers and cause a series of problems, such as tension, anchorage, relaxation of

the prestressed tendons, etc. In addition, it will lead to excessive elastic deformations of prestressed tendons, and the maximum deformations of dampers will be limited. Concurrently, there is significant worry over another type of self-centering damper. These dampers use mechanisms that compress disc springs or ring springs to drive them to recenter. Research about its mechanical behavior and the performance of shock absorption has been carried out. Xu and Fan et al. [17–19] combined the pre-pressed disc springs and FD into a self-centering energy dissipation brace, conducted the experiments, and established an axial force formula. Filiatrault et al. [20] proposed a self-centering friction energy dissipation device for reducing the earthquake responses of buildings based on the friction hysteresis of ring springs and conducted prototype tests of dampers to observe their practical mechanical behavior. Khoo et al. [21,22] used ring springs to reduce the residual deformations of sliding hinge joints and conducted prototype tests of self-centering joints.

A shape memory alloy (SMA) has the good performance of self-centering and energy dissipation simultaneously, and its plastic deformation caused by external loads will rapidly dissipate after unloading [23]. Under cyclic load, SMA can also disperse the input energy, which is suitable for the advancement of self-centering energy dissipation devices. Qian et al. [24] proposed a self-centering damper-based SMA wire and investigated how the pre-strain of SMA affects the hysteretic performance of the damper through tests. Shi et al. [25–28] developed a self-centering energy dissipation brace based on SMA cables and proved that its hysteretic performance and mitigation for structural seismic responses were, respectively, researched through mechanical experiments and finite element analysis. The FD can effectively dissipate the energy input from an earthquake and protect the components of buildings [29]. Thus, the means of developing self-centering dampers by combining SMA with FD has attracted much attention. Li et al. [30] proposed a self-centering FD by connecting the SMA rods in parallel with the FD, and then the corresponding mechanical tests and parameter analysis were conducted. Chen and Qiu et al. [31,32] developed a self-centering variable FD in which the SMA elements provided the pre-tightening force for variable FD and drove the damper to recenter simultaneously. Zheng et al. [33,34] proposed a self-centering isolator with SMA to mitigate the seismic response of bridges.

In February 2023, earthquakes with a magnitude of 7.8 and 7.6 occurred in southeast Turkey successively, just nine hours apart [35]. Multiple aftershocks are frequently felt in response to a mainshock, and mainshock–aftershock sequences (MS-AS) can cause structural damage to accumulate and quickly put the structure in a more risky state. For that reason, lots of scholars have considered MS-AS when investigating the seismic performance of structures. Lu et al. [36] proposed a method for the seismic damage prediction of regional buildings that took into account MS-AS. Raghunandan et al. [37] analyzed the aftershock vulnerability of reinforced concrete (RC) frames and found that the collapse resistance capacities of buildings would decrease with the strength of MS increasing. Wen et al. [38] proposed MS-AS damage spectra at soft soil sites. Yu et al. [39] found that the AS reduced the collapse resistance capacity through the MS-AS vulnerability analysis of inelastic single-degree-of-freedom systems. Zhou et al. [40] established a seismic demand model for RC structures and the corresponding formula for estimation of earthquake fragilities, which showed that the MS-AS would improve the exceedance probability of buildings.

To achieve the recentering effect, the traditional self-centering damper-based SMAs need a large consumption of SMA, which leads to a high cost. Thus, this study suggested using coil springs and SMA in a dual self-centering (D-SC) drive mode with a low cost. A novel dual self-centering friction damper (D-SCFD) design was put into practice. Through small-scale mechanical testing, the impacts of pre-tightening force and loading displacement amplitudes on D-SCFD's energy dissipation and recentering performance were examined. The parameter study was conducted using the simplified mechanical model of D-SCFD as well as existing index formulas for energy dissipation performance and recentering. Lastly, the seismic response control impacts of D-SCFD with variable

recentering performance on SF under MS-AS were examined using a multi-story steel frame (SF) as the analytical object.

## 2. Design of D-SCFD

### 2.1. Configuration of D-SCFD

The main functional elements of D-SCFD are coil springs, SMA rods, and FD with two sliding surfaces. The D-SC was formed after the connection of coil springs in parallel with SMA rods. The components of the D-SCFD were as follows: an internal panel, asbestos friction sheets, external panels with coil spring anchor plates, high-strength bolts, high-strength nuts, SMA rods, coil springs, guide bars, and a connection block for connecting the two external panels. The configuration of the D-SCFD is shown in Figure 1.

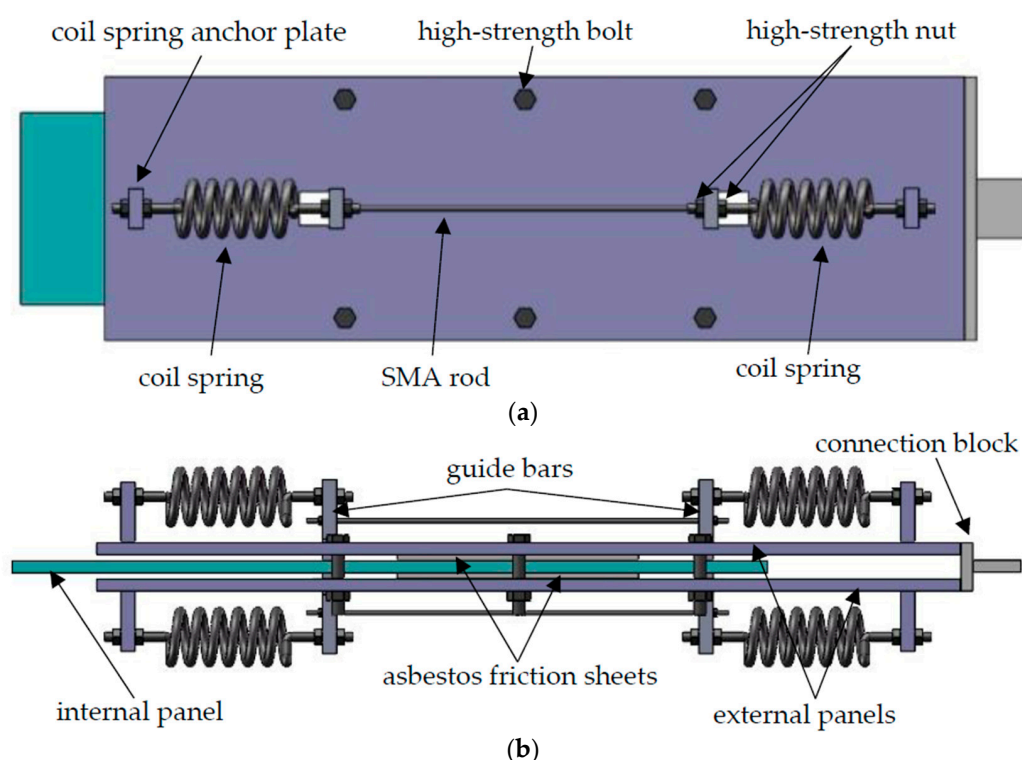


**Figure 1.** Configuration of D-SCFD: (a) planform and (b) side view.

During the assembly process of the FD, two asbestos friction sheets were, respectively, fixed on the upper and lower surfaces of the internal panel and kept sliding with the external panels. Screw holes were saved on both sides of the external panels, and the friction sheets were pre-tightened using high-strength bolts. For the D-SC, the two ends of the guide bars had reserved holes for the anchorages of the SMA rods and the coil springs. After the two guide bars, respectively, passed through the corresponding slots reserved at both ends of the three panels, the two guide bars were connected by SMA rods. The two ends of the SMA rods were anchored to the guide bars by high-strength nuts. Each guide bar was attached to the matching anchor plate on the external panels by two pairs of coil springs. High-strength nuts were also used to secure the ends of coil springs. Finally, the connection block was welded to one end of the external panels to complete the D-SCFD system.

### 2.2. Working Principle of D-SCFD

In the process of the reciprocating motion of the D-SCFD, the SMA rods were always alternately in two states of tension and recentering. Meanwhile, the coil springs on one side were alternately in two states of compression and recentering. The axial force response

of D-SC inhibited the deformation of D-SCFD during loading. In the unloading process, the restoring force of D-SC was composed of the elastic force of coil springs and the transformation stress of SMA rods, which drove the D-SCFD to recenter by overcoming the frictional force generated by the FD.

The working principle of D-SCFD is shown in Figure 2. When the external excitation caused the tensile deformation of the damper, the relative displacement between the internal panel and the external panels occurred. It also caused sliding friction between the friction sheets and the external panels, dissipating the energy intake from seismic excitation. The internal panel simultaneously pushed the guide bar on one side while the guide bar on the other side was stationary relative to the external panels, stretching the SMA rods and compressing the coil springs on one side. When the D-SCFD was compressed, the guide bar on one side remained motionless in relation to the external panels, while that on the other was pushed by the internal panel. It compressed the coil springs on the other side while stretching the SMA rods. The force for the recentering of the damper was provided by coil springs and SMA rods, reducing the consumption of SMA rods.

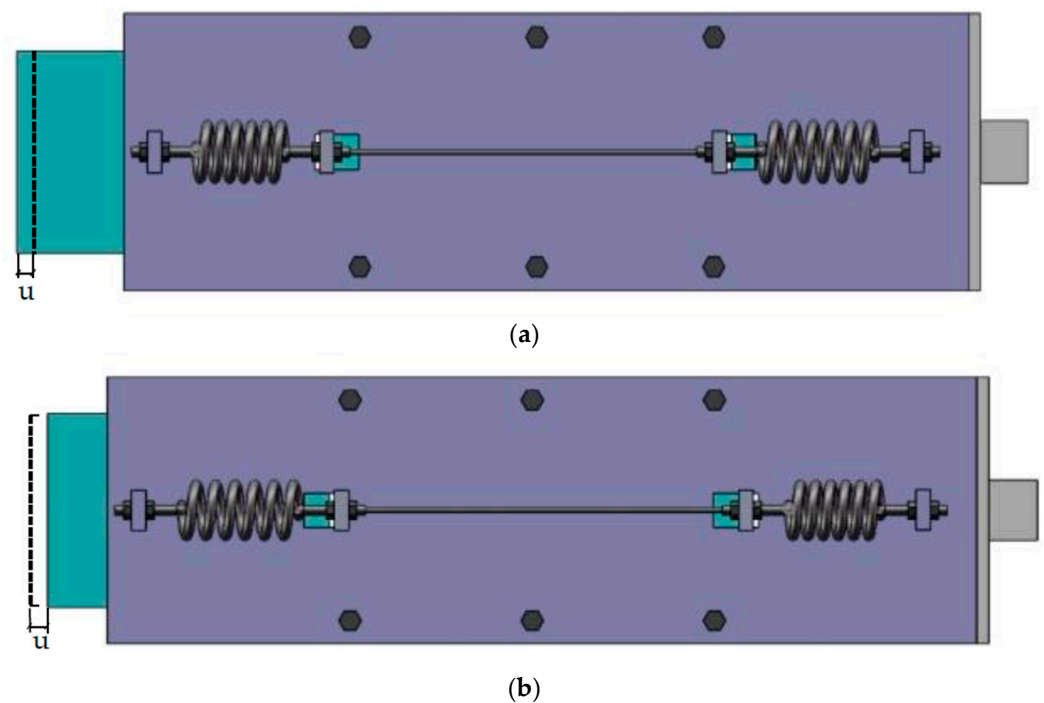


**Figure 2.** Working principle of D-SCFD: (a) tension state and (b) compression state, where  $u$  denotes the axial deformation.

### 3. Test

#### 3.1. Tensile Test of SMA

According to the literature [32], the mechanical properties of SMA tend to be stable after cyclic tensile loading. Therefore, before the test of D-SCFD, the SMA rod with a diameter of 4 mm was trained 20 times under equal-amplitude cyclic tensile loading, which made the mechanical properties of the SMA rod stable. The contents of nickel and titanium in the SMA rod were 50.1% and 49.9%, respectively. Meanwhile, the transformation stress and strain of SMA rods were obtained by the cyclic tensile test under variable amplitude loading. The loading rate of the tensile tests was set to 5 mm/min, and the ambient temperature was 15 °C. The parameters of the tensile test conditions are shown in Table 1, and the corresponding loading equipment is shown in Figure 3.

**Table 1.** Tensile test conditions of the SMA rod.

No.	Section Area of SMA (mm <sup>2</sup> )	Loading Rate (mm/min)	Number of Loading Cycles	Strain Amplitude (%)
1	12.57	5	20	5
2	12.57	5	1	3.57

**Figure 3.** Loading equipment of the SMA rod.

As shown in Figure 4, the constitutive curves from the results of the tensile test revealed that the residual strain of the SMA rod reached 1.98% after the first tension. In the subsequent cyclic tensile test under equal amplitude loading, the residual strain became small, indicating that the SMA rod had a good capacity for self-centering. With the increase in the number of loading cycles, the SMA stress gradually decreased and tended to be stable. The maximum stresses of SMA rods in the 14th and 20th tensile tests were 452.38 MPa and 446.46 MPa, respectively. The relative difference between both was only 1.33%, and the amplitude of the fluctuations was small. The stress of the SMA rod increased linearly with the strain increases in the cyclic tensile test under varying amplitude loadings, and subsequently, the stress increased at a slower rate when the martensitic transformation occurred. In the unloading process, the SMA rod with a different initial strain had stress–strain curves with three different kinds of slopes, and the descent rate of stress was lowest during the reverse martensitic transformation of SMA. The stress–strain curves from the tensile tests showed that the SMA rod had good superelastic properties, and the mechanical properties after tensile training were less affected by the loading times. The transformation stress and strain of SMA with the maximum tensile strain of 7% are shown in Table 2.

**Table 2.** Transformation stress and strain of the SMA rod.

$\sigma_{Ms}$ (MPa)	$\epsilon_{Ms}$ (%)	$\sigma_{Mf}$ (MPa)	$\epsilon_{Mf}$ (%)	$\sigma_{As}$ (MPa)	$\epsilon_{As}$ (%)	$\sigma_{Af}$ (MPa)	$\epsilon_{Af}$ (%)
454.19	1.82	609.89	6.97	271.78	5.29	116.08	0.47

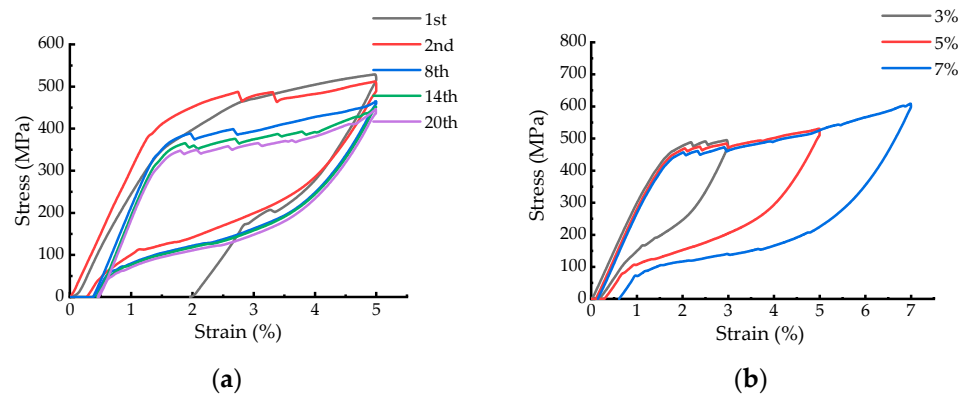


**Figure 4.** Stress–strain curves from the tensile test of the SMA rod: (a) under equal amplitude loading and (b) under variable amplitude loading.

### 3.2. Mechanical Test of D-SCFD

To study the effects of the loading displacement amplitude and FD's pre-tightening force on the mechanical properties of D-SCFD, a small-scale specimen with the maximum permissible deformation of 21 mm was fabricated according to the configuration described earlier, and the mechanical tests of FD and D-SCFD were conducted under low-reversed cyclic loading. The material of the friction sheets was composed of asbestos and brass wires in FD. The SMA rods after tensile training were installed in D-SCFD, whose working length was 300 mm. For the coil springs, the diameter of the spring wire was 8 mm, the outer diameter was 50 mm, and the axial stiffness was 145 N/mm. The material of the coil springs was Mn-Cr Alloy (Mn 1.02%, Cr 0.29%). The tensile strength of the high-strength bolts and nuts was 1200 MPa, and the diameter of the screw was 10 mm. The rest of D-SCFD adopted the steel with a yield strength of 235 MPa. The specimen, test conditions, and test device are shown in Figure 5, Table 3, and Figure 6, respectively. The ambient temperature was 15 °C.



**Figure 5.** Specimen of D-SCFD.

**Table 3.** Test conditions of D-SCFD.

No.	ID of Specimen	Section Area of SMA (mm <sup>2</sup> )	Loading Rate (mm/min)	Loading Displacement Amplitude (mm)	Pre-Tightening Force of FD (kN)
1	FD	0	5	9 15 21	7
2	D-SCFD	25.13	5	9 15 21	3 5 7

The hysteretic curves of FD with a pre-tightening force of 7 kN are shown in Figure 7. The axial force generated by FD was stable, and the hysteretic curves under different loading displacement amplitudes were rectangular in shape. The areas of hysteretic curves increased with the increase in the axial deformation of FD. According to the results from the tests of FD and the configuration with two sliding surfaces, the coefficient of sliding friction was 0.50, which was denoted by  $\mu$ . As shown in Figure 8, the shapes of the hysteretic curves of D-SCFD were similar to those of the stress–strain curves of SMA, both of which

are “flag-shape”. The axial force of D-SCFD fluctuated slightly at the start of the martensitic transformation of SMA rods during loading and became stable gradually with the increase in the axial deformation. The areas of the hysteretic curves of D-SCFD also increased while the pre-tightening force of FD increased, and they were positively correlated with the axial deformation. After the pre-tightening force of FD was magnified, the horizontal coordinates of hysteretic curves with an axial force of 0 kN increased during unloading, indicating that the residual deformation of D-SCFD increased. The hysteretic curves from the test of D-SCFD reflected that the performance of energy dissipation could be improved by magnifying the axial force responses of FD, but the performance of recentering would be adversely affected.



**Figure 6.** Test devices of D-SCFD: (a) loading device and (b) data acquisition device.

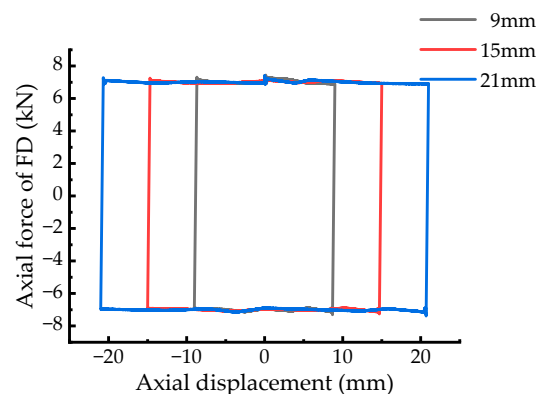


**Figure 7.** Hysteretic curves of FD.

The mechanical property parameters, such as dissipated energy, secant stiffness, equivalent viscous damping, and the rate of residual deformation, denoted by  $W$ ,  $K$ ,  $\zeta_{eq}$ , and  $R_{dr}$ , respectively, were used to measure the performance of D-SCFD in this study. The mechanical property parameters of D-SCFD are shown in Figure 9. The  $\zeta_{eq}$  of D-SCFD fluctuated with the increase in axial deformation, the maximum variation of which only reached 2.37%. Thus, the  $\zeta_{eq}$  of D-SCFD was less affected by the loading displacement amplitude. The relative increment of  $W$  was close to that of the strain energy, which was caused by the increase in the axial deformation of D-SCFD. That was the main reason why the  $\zeta_{eq}$  of D-SCFD was less affected by the loading displacement amplitude. Wherein, the strain energy of D-SCFD is  $KD^2/2$ , and  $D$  denotes the axial deformation of D-SCFD. The  $\zeta_{eq}$  of D-SCFD increased with the magnification of the pre-tightening force of FD, indicating

that the relative increment of  $W$  caused by magnifying the pre-tightening force of FD was greater than that of strain energy.

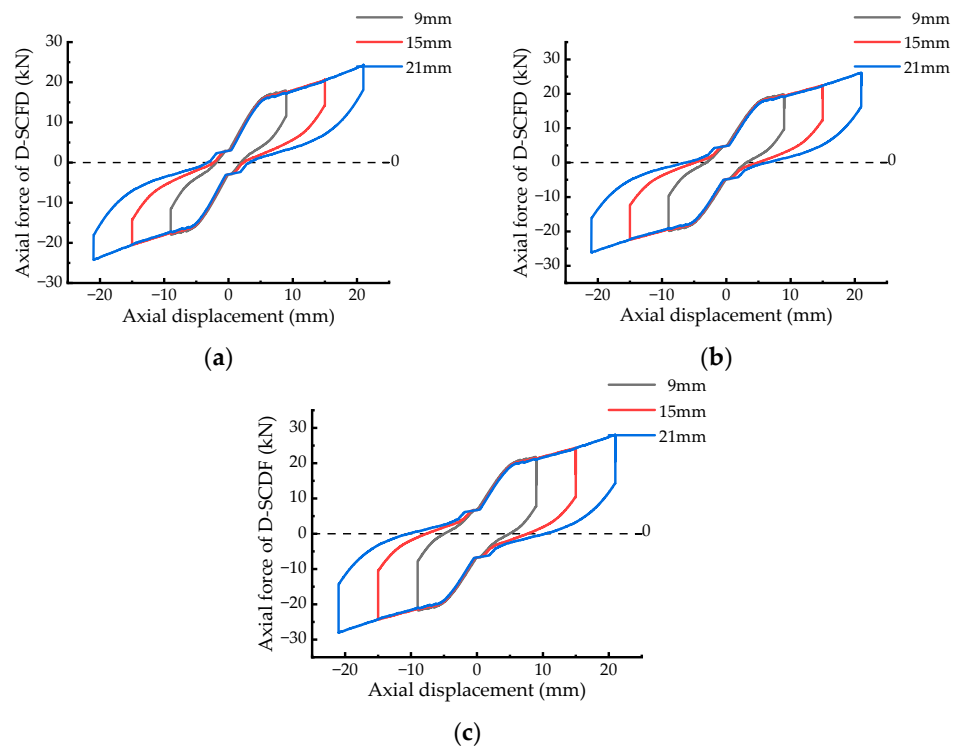


**Figure 8.** Hysteretic curves of D-SCFD: (a) pre-tightening force of FD is 3 kN, (b) pre-tightening force of FD is 5 kN, and (c) pre-tightening force of FD is 7 kN.

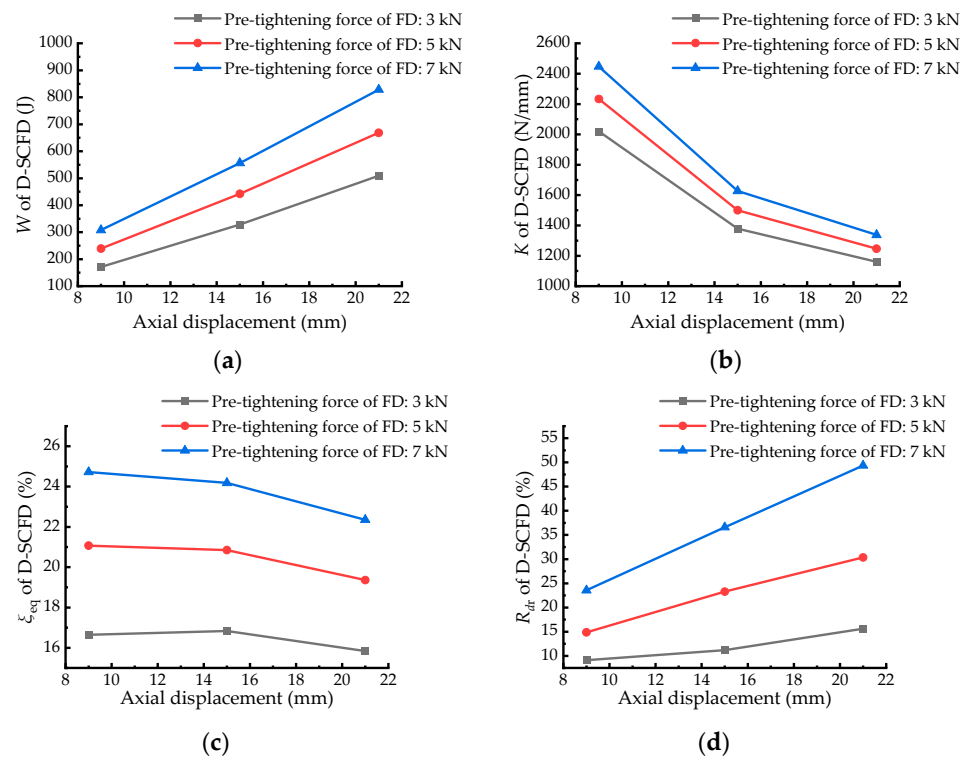


**Figure 9.** Mechanical property parameters of D-SCFD: (a) dissipated energy, (b) secant stiffness, (c) equivalent viscous damping, and (d) rate of residual deformation.

The  $R_{dr}$  of D-SCFD increased after magnifying the pre-tightening force of FD, and the maximum value of  $R_{dr}$  reached 49.35%. The slope of each force–deformation curve of D-SCFD decreased with the increase in axial deformation when SMA underwent reverse martensitic transformation. This indicates that the amplification of  $R_{dr}$  was positively correlated with the axial deformation. The experimental results of D-SCFD showed that the performance of energy dissipation was less affected by the axial deformation after the martensitic transformation of SMA happened but more affected by the pre-tightening force of FD. Meanwhile, the recentering performance of D-SCFD was negatively correlated with the pre-tightening force of FD, whose reduction caused by magnifying the pre-tightening force of FD became more obvious with the increase in axial deformation.

#### 4. Simplified Mechanical Model and Parameter Analysis

##### 4.1. Verification of Simplified Mechanical Model

A simplified mechanical model of D-SCFD was established to analyze the influence of coil springs, SMA rods, and FD on the performance of recentering and energy dissipation. In the model, the relations of restoring force provided by those elements could be acquired, which meet the requirements related to different performance objectives of recentering. Meanwhile, the accuracy of the simplified mechanical model was verified according to the experimental results. The simplified analysis model is shown in Figure 10. D-SCFD was generated in parallel by coil springs, SMAs, and FD, and the axial force response was the sum of that provided by each element.

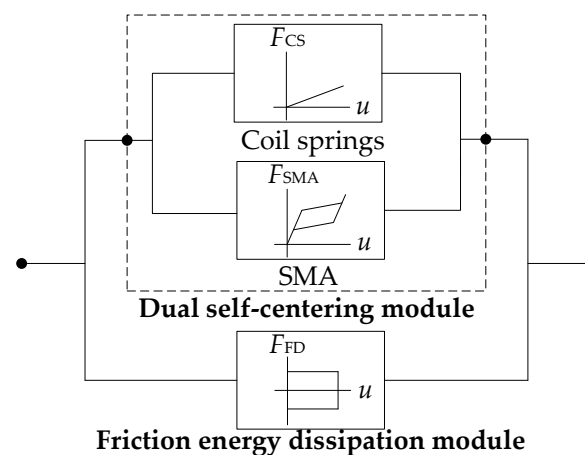


Figure 10. Schematic diagram of D-SCFD simplified analysis model.

Referring to the previous study [41], the axial force of SMA rods is calculated by a piecewise linear algorithm here. In addition, we ignored the difference in the elastic modulus between the austenitic and martensitic phases of SMA rods. Compared with the SMA mechanical model proposed by Brinson and Auricchio [42,43], the suggested model in this study needs a lower computational cost. The convenient calculations of  $R_{dr}$  and  $\zeta_{eq}$  can be derived from this model, too. The axial force of D-SCFD can be calculated by the following:

$$F_{D-SCFD} = k_{CS}u + P\mu\text{sgn}\left(\frac{du}{dt}\right) + F_{SMA} \quad (1)$$

where  $F_{D-SCFD}$  is the axial force response of D-SCFD;  $k_{CS}$  denotes the total stiffness of the coil springs;  $u$  is the axial deformation of D-SCFD;  $t$  denotes the time;  $P$  and  $\mu$  are the pre-tightening force and sliding friction coefficient of FD, respectively;  $\text{sgn}(x)$  is a symbolic function that returns either 1 or  $-1$ , depending on the positivity or negativity of  $x$ ;  $F_{SMA}$  is the axial force of the SMA rods, and the value can be derived from the following:

$$F_{SMA} = \varepsilon\left(u\frac{du}{dt}\right)F_{SMA}^L + \varepsilon\left(-u\frac{du}{dt}\right)F_{SMA}^U \quad (2)$$

where  $\varepsilon(x)$  is a step function and returns 0, 1/2, or 1 according to the relationship between  $x$  and 0;  $F_{SMA}^L$  and  $F_{SMA}^U$  are the axial force responses of SMA rods during loading and unloading, respectively, which can be calculated by the following:

$$F_{SMA}^L = \begin{cases} k_{SMA,1}u, & |u| \leq u_{Ms} \\ \text{sgn}(u)[k_{SMA,2}(|u| - u_{Ms}) + F_{Ms}], & u_{Ms} < |u| \leq u_{Mf} \end{cases} \quad (3)$$

$$F_{SMA}^U = \begin{cases} k_{SMA,1}u, & |u| \leq u_{Af} \\ \text{sgn}(u)[k_{SMA,2}(|u| - u_{Af}) + F_{Af}], & u_{Af} < |u| \leq u'_{AS} \\ \text{sgn}(u)[k_{SMA,1}(|u| - u'_{UL}) + F_{UL}^S], & u'_{AS} < |u| \leq u_{UL}^S \end{cases} \quad (4)$$

where  $k_{SMA,1}$  and  $k_{SMA,2}$  denote the linear stiffness of SMA rods before and after martensitic transformation, respectively;  $u_{Ms}$  and  $F_{Ms}$  are the axial deformation and force of SMA rods at the start of martensitic transformation, respectively.  $u_{Mf}$  denotes the axial deformation of SMA rods at the end of martensitic transformation.  $u_{Af}$  and  $F_{Af}$  are the axial deformation and force at the end of the reverse martensitic transformation of SMA rods, respectively.  $u_{UL}^S$  and  $F_{UL}^S$  are the axial deformation and force of SMA rods at the beginning of unloading, respectively, which can be calculated by way of  $F_{SMA}^L$ .  $u'_{AS}$  represents the axial deformation of SMA rods at the point of where reverse martensitic transformation begins, whose calculation is given as below:

$$u'_{AS} = \frac{F_{Af} - F_{UL}^S - k_{SMA,2}u_{Af} + k_{SMA,1}u_{UL}^S}{k_{SMA,1} - k_{SMA,2}} \quad (5)$$

When the axial deformation of D-SCFD reaches the maximum permissible value, the rate of residual deformation and equivalent viscous damping derived from the simplified mechanical model are expressed as below:

$$R_{dr} = \begin{cases} \frac{\beta}{\alpha + \frac{\sigma_{Ms}^{\varepsilon_{Mf}}}{\sigma_{Mf}^{\varepsilon_{Ms}}}}, & F_{FD} \leq F_{CS} \frac{\varepsilon_{Af}}{\varepsilon_{Mf}} + F_{Mf} \frac{\sigma_{Af}}{\sigma_{Mf}} \\ \beta + \frac{(\sigma_{Mf} - \sigma_{Ms})\varepsilon_{Af} - \frac{\sigma_{Af}}{\sigma_{Mf}}}{\alpha + \frac{(\sigma_{Mf} - \sigma_{Ms})\varepsilon_{Mf}}{\sigma_{Mf}(\varepsilon_{Mf} - \varepsilon_{Ms})}}, & F_{CS} \frac{\varepsilon_{Af}}{\varepsilon_{Mf}} + F_{Mf} \frac{\sigma_{Af}}{\sigma_{Mf}} < F_{FD} \text{ \& } \\ & F_{FD} \leq F_{CS} \frac{\varepsilon_{As}}{\varepsilon_{Mf}} + F_{Mf} \frac{\sigma_{As}}{\sigma_{Mf}} \\ \frac{\beta + \frac{\sigma_{Ms}^{\varepsilon_{Mf}}}{\sigma_{Mf}^{\varepsilon_{Ms}}}}{\alpha + \frac{\sigma_{Ms}^{\varepsilon_{Mf}}}{\sigma_{Mf}^{\varepsilon_{Ms}}}}, & F_{CS} \frac{\varepsilon_{As}}{\varepsilon_{Mf}} + F_{Mf} \frac{\sigma_{As}}{\sigma_{Mf}} < F_{FD} \end{cases} \quad (6)$$

$$\zeta_{eq} = \frac{2\left(\frac{\varepsilon_{Mf} - \varepsilon_{Ms}}{\varepsilon_{Mf}}\right)\left[\frac{\sigma_{Ms} - \sigma_{Af}}{\sigma_{Mf}} - \frac{(\sigma_{Mf} - \sigma_{Ms})(\varepsilon_{Ms} - \varepsilon_{Af})}{\sigma_{Mf}(\varepsilon_{Mf} - \varepsilon_{Ms})}\right] + 4\beta}{2\pi(1 + \alpha + \beta)} \quad (7)$$

where  $\alpha$  denotes the ratio of the axial force of the coil springs to that of SMA rods when the axial deformation of D-SCFD reaches the maximum permissible value;  $\beta$  is the ratio of the axial force of FD to that of SMA rods in the same situation.  $F_{CS}$  represents the maximum axial force of the coil springs.

Combined with the tensile test results of SMA, the hysteretic curves of D-SCFD were predicted using the simplified mechanical model outlined here. The comparison of hysteretic curves between the predicted and experimental results is shown in Figure 11. The main parameters of the simplified mechanical model are listed in Table 4. The axial force responses with the double lines computed by the simplified model during loading fit well with the test findings. In the unloading, there were small differences in  $F_{D-SCFD}$  between the predicted and experimental values. The simplified model ignored the distinction of elastic modulus between the austenitic and martensitic phases of SMA and did not consider that the stress–strain curves had the characteristics of “smooth transition” at the start of reverse martensitic transformation. That was the main reason behind the prediction of  $F_{D-SCFD}$  deviating from the experimental results during unloading.

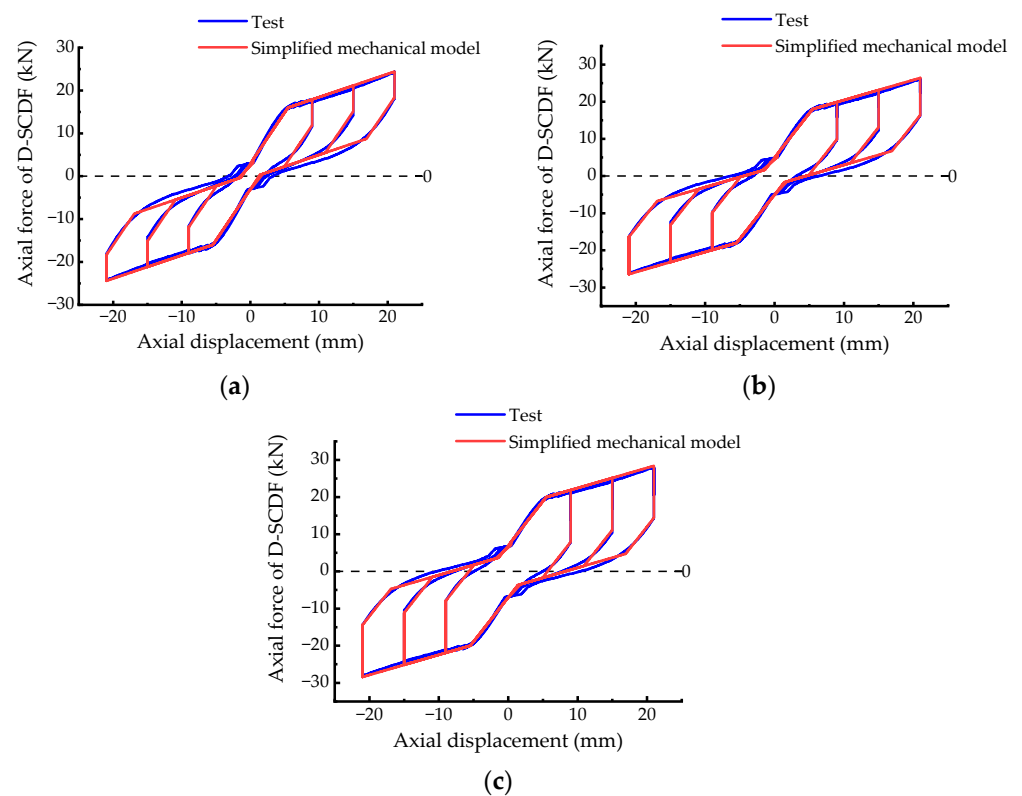


**Figure 11.** Comparison of hysteretic curves between the predicted and experimental results: (a) pre-tightening force of FD is 3 kN, (b) pre-tightening force of FD is 5 kN, and (c) pre-tightening force of FD is 7 kN.

**Table 4.** Parameters of the mechanical model.

$u_{Ms}$ (mm)	$F_{Ms}$ (N)	$u_{Mf}$ (mm)	$F_{Mf}$ (N)	$u_{Af}$ (mm)	$F_{Af}$ (N)	$k_{SMA,1}$ (N/mm)	$k_{SMA,2}$ (N/mm)
5.47	11,409.18	21.00	15,328.21	1.40	2915.95	2085.77	251.84

The maximum difference in  $F_{D-SCFD}$  between the predicted and the experimental values was only 2.93 kN, which is acceptable. When the axial deformation of D-SCFD reached the maximum permissible value, a comparative analysis of the theoretical and experimental values of  $R_{dr}$  and  $\zeta_{eq}$  was conducted, as presented in Table 5. The corresponding maximum absolute error was only 10.27% and 0.81%, respectively. Therefore, the calculation methods of  $R_{dr}$  and  $\zeta_{eq}$  derived from the simplified mechanical model can describe the recentering and energy dissipation performance of D-SCFD.

**Table 5.** Comparison of theoretical and experimental values of  $R_{dr}$  and  $\zeta_{eq}$ .

Pre-Tightening Force of FD (kN)	Theoretical $R_{dr}$ (%)	Experimental $R_{dr}$ (%)	Absolute Error of $R_{dr}$ (%)	Theoretical $\zeta_{eq}$ (%)	Experimental $\zeta_{eq}$ (%)	Absolute Error of $\zeta_{eq}$ (%)
3	6.03	15.63	9.6	15.03	15.84	0.81
5	21.48	30.35	8.87	18.72	19.36	0.64
7	39.08	49.35	10.27	21.89	22.35	0.46

#### 4.2. Parameter Analysis

The methods introduced earlier were used to calculate the  $R_{dr}$  and  $\zeta_{eq}$  with different  $\alpha$  and  $\beta$ . The  $\alpha$  was used to describe the ratio of axial force provided by coil springs and

SMA rods. The  $\beta$  measured the ratio of axial force provided by the FD and SMA rods. While the total force of the damper is constant, the consumption of SMA can decrease with an increase in  $\alpha$  and  $\beta$ . Based on that, the variation trends of recentering and energy dissipation performance of D-SCFD were further analyzed, which are shown in Figure 12. The value of  $\alpha$  ranged from 0 to 100%. When the  $\alpha$  was 0, the variation trend of  $R_{dr}$  had three different growth rates with the increase in  $\beta$ . This also indicated that continuing to magnify the  $F_{FD}$  would result in a significant increase in  $R_{dr}$  in the absence of coil springs, especially in the case where the  $F_{FD}$  exceeded  $F_{Af}$ . After increasing  $\alpha$ , the growth rate of  $R_{dr}$  relative to  $\beta$  gradually decreased, which indicated that coil springs could improve the recentering performance of D-SCFD.  $\zeta_{eq}$  rose with the increase in  $\beta$ , and the growth rate decreased gradually. However, magnifying  $\alpha$  led to a decrease in  $\zeta_{eq}$ , the amplitude of which decreased gradually. The variation trends of  $R_{dr}$  and  $\zeta_{eq}$  appeared, suggesting that improving the recentering performance will bring about a decrease in the energy dissipation performance, both of which are contradictory. Therefore, the proportion of restoring forces provided by coil springs, SMA, and FD is critical, as it is a requirement for D-SCFD to work optimally in terms of both recentering and energy dissipation.

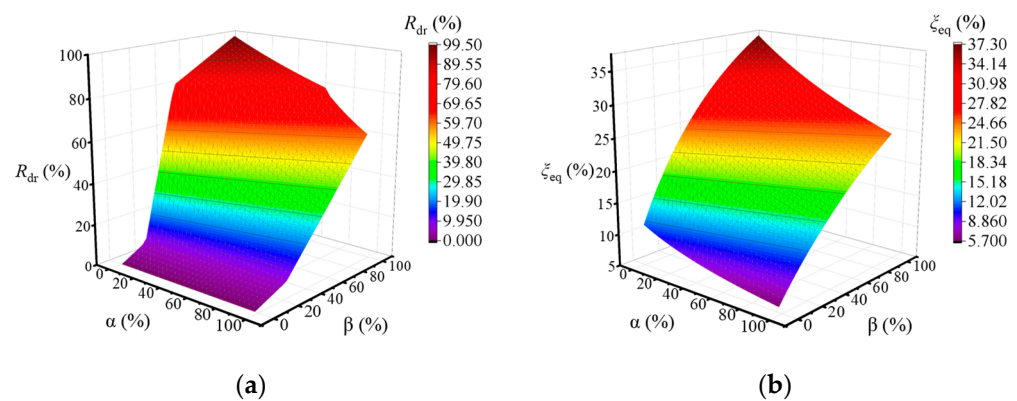


**Figure 12.** Variation trends of recentering and energy dissipation performance: (a)  $R_{dr}$  and (b)  $\zeta_{eq}$ .

Firstly, the relationship between  $\alpha$  and  $\beta$  was determined by the calculation method of  $R_{dr}$ , which can achieve three different performance targets for recentering. Then, the influence of the corresponding  $\alpha$  and  $\beta$  on the energy dissipation performance of D-SCFD was analyzed. When the  $R_{dr}$  was 10%, 30%, and 50%, the relationship between  $\alpha$  and  $\beta$  satisfied the equation as below:

$$\beta = \begin{cases} \frac{\alpha}{10} + 0.2016, & R_{dr} = 10\% \\ \frac{3\alpha}{10} + 0.2707, & R_{dr} = 30\% \\ \frac{5\alpha}{10} + 0.3398, & R_{dr} = 50\% \end{cases} \quad (8)$$

Combining the relation equation and calculation method of  $\zeta_{eq}$ , the curves of  $\zeta_{eq}$  with different targets of recentering performance of D-SCFD are shown in Figure 13. The  $\zeta_{eq}$  of D-SCFD decreased with the increase in  $\alpha$  and a reduction in  $\zeta_{eq}$  gradually rose with the decrease in  $R_{dr}$ . When  $R_{dr}$  was 10%, 30%, and 50%, respectively, the corresponding maximum reduction in  $\zeta_{eq}$  was 6.87%, 3.97%, and 1.83%, respectively. Therefore, when the high recentering performance target is taken, it is inappropriate to choose a larger ratio of axial force of coil springs to that of SMA, which can avoid a sharp decline in the energy dissipation performance of the D-SCFD. As the recentering performance target decreases, that ratio can be magnified appropriately, reducing the consumption of SMAs.

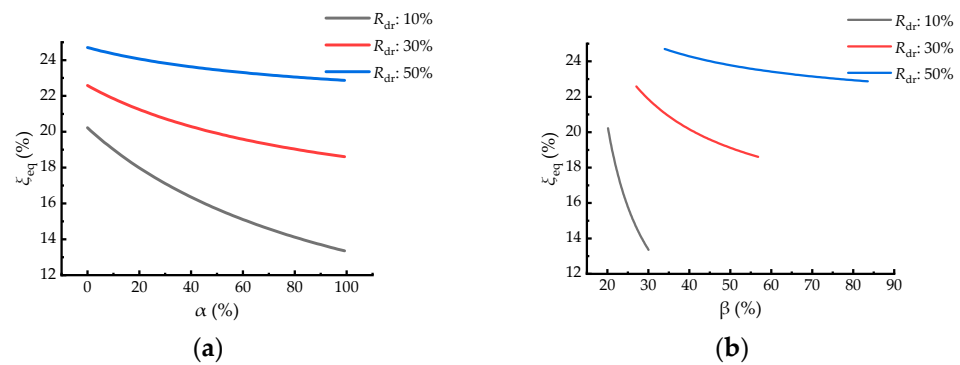


**Figure 13.** Variation trends of  $\zeta_{eq}$  with different performance of recentering: (a) influence of  $\alpha$  and (b) influence of  $\beta$ .

## 5. Seismic Response Mitigation of Multi-Story SF

### 5.1. Overview of Structure Case

A five-story steel frame (SF) is selected as the case, which is located in Jiangsu Province, China. The control effects of D-SCFD on the seismic responses of SF were obtained by nonlinear time history analysis, considering the different recentering performances of D-SCFD. The structural plane of SF is shown in Figure 14. The members of SF adopted steel with a yield strength of 355 MPa, the design of which considered earthquake action according to the Chinese code for seismic design of buildings (GB 50011-2010) [44]. Its beams and columns will not yield after experiencing frequently occurred earthquakes (FOE). According to the Chinese code for seismic design of buildings [44], the  $S_a(0.74\text{ s}, 4\%)$  and  $S_a(0.74\text{ s}, 5\%)$  of the SF under FOE and maximum considered earthquake (MCE) are 0.19 g and 0.91 g, respectively. Here,  $S_a(T_1, \zeta)$  denotes the spectral acceleration corresponding to the first translational period of SF, and the letter g denotes the gravitational acceleration.

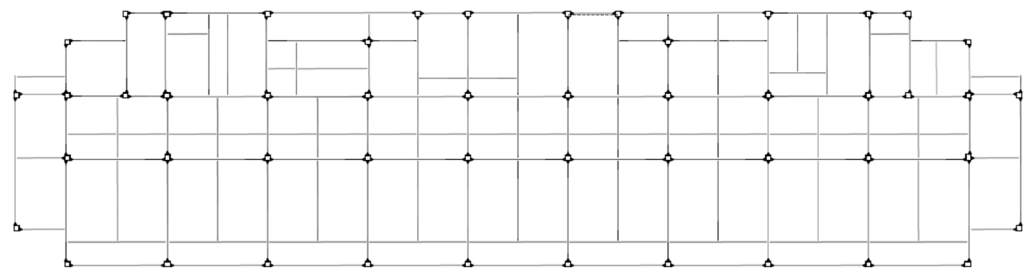


**Figure 14.** Structural plane of SF.

### 5.2. Ground Motion Inputs

The previous studies [36–40] reflected that the MS-AS would lead to the accumulation of structural damage and that the AS should be considered in the control of structural seismic responses. Therefore, seven groups of MS-AS records were selected as the excitation, and the directions of inputs were the same as those of the first translational vibration mode of SF. The information about each ground motion is listed in Table 6. When compared to  $S_a(T_1, \zeta)$ , using the peak ground acceleration (PGA) to characterize the intensities of ground motions readily makes structure responses more distinct [45]. Based on the  $S_a(0.74\text{ s}, 5\%)$  being 0.91 g when SF experiences MCE, the accelerations of all ground motions were adjusted accordingly. Meanwhile, time intervals of 20 s were added between the MS and AS, and durations of 10 s were added to the ends of the AS to analyze the residual deformations of the structure. The acceleration and response spectra curves are shown in Figure 15 and Figure 16, respectively.

Table 6. Information about ground motions.

No.	Event	MS		AS		Station
		Earthquake Magnitude (Mw)	Date	Earthquake Magnitude (Mw)	Date	
GM1	Chalfant Valley	5.77	20 July 1986	6.19	21 July 1986	Bishop, Paradise Lodge
GM2	Whittier Narrows	5.99	1 October 1987	5.27	4 October 1987	Bell Gardens, Jaboneria
GM3	Northridge	6.69	17 January 1994	5.28	20 March 1994	Arleta, Nordhoff Fire Sta
GM4	Chi-Chi, Taiwan	7.62	20 September 1999	6.20	20 September 1999	CHY024
GM5	L'Aquila, Italy	6.30	6 April 2009	5.60	7 April 2009	L'Aquila, Parking
GM6	Darfield, New Zealand	7.00	3 September 2010	6.20	21 February 2011	Canterbury Aero Club
GM7	Kahramanmaras, Turkey	7.70	6 February 2023	7.60	6 February 2023	6203

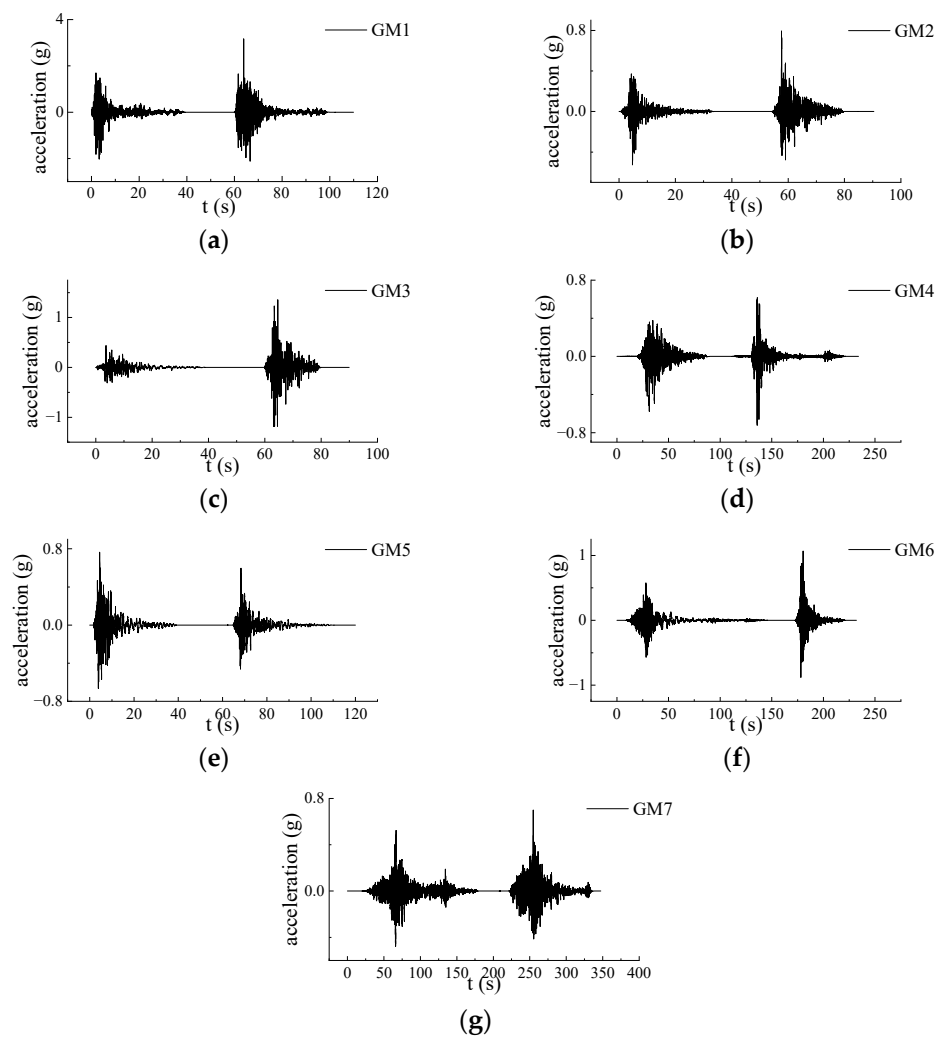


Figure 15. Acceleration of ground motions: (a) GM1, (b) GM2, (c) GM3, (d) GM4, (e) GM5, (f) GM6, and (g) GM7.

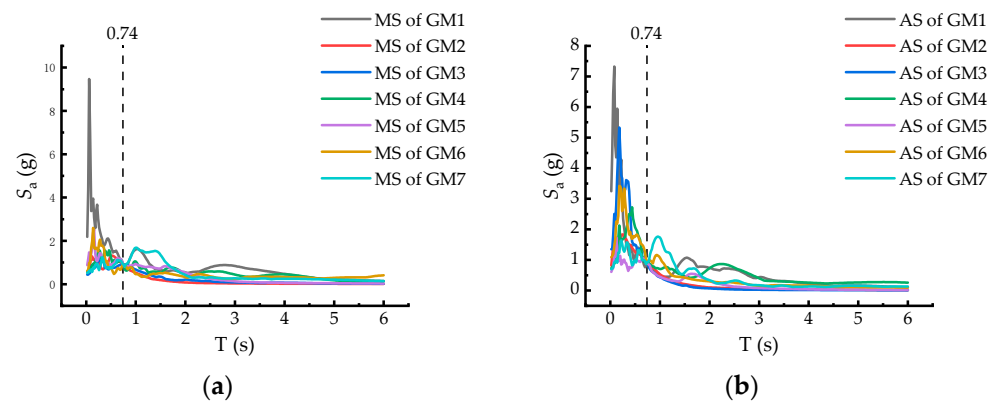


Figure 16. Response spectra of ground motions: (a) MS and (b) AS.

### 5.3. D-SCFD

To analyze the seismic response control effects of D-SCFD with different recentering performances, D-SCFDs with  $R_{dr}$  values of 10%, 30%, and 50% were used to mitigate the seismic responses of SF, respectively. The layout of the D-SCFDs on each floor is shown in Figure 17.

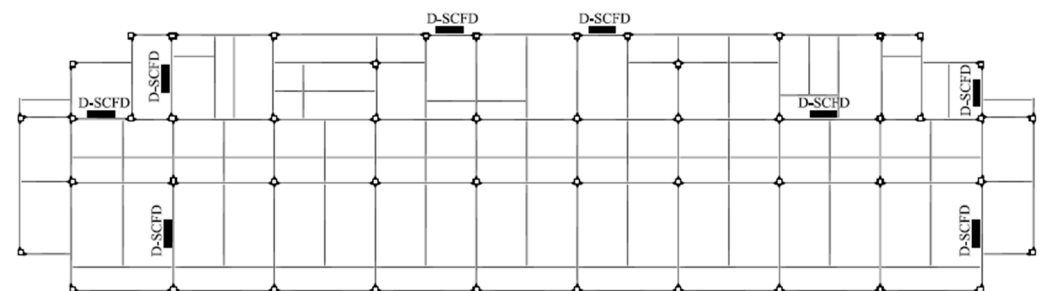


Figure 17. Plane layout of D-SCFDs.

In addition to one damper at each corresponding plane position of the top two floors, two dampers were set on each of the other floors. The  $\alpha$  of D-SCFD was taken as 20%, and the  $\beta$  corresponding to the three different recentering performances was obtained earlier using the relation equation mentioned. The maximum axial forces of all D-SCFDs were 500 kN, whose limits of deformation were 60 mm based on the maximum inter-story drift responses of SF under the MCE. The main design parameters of D-SCFD are listed in Table 7.

Table 7. Design parameters of D-SCFD.

No.	ID of Damper	Maximum Axial Force (kN)	Limits of Deformations (mm)	$\alpha$ (%)	$\beta$ (%)	Theoretical $\zeta_{eq}$ (%)	Theoretical $R_{dr}$ (%)	Section Area of SMA (mm <sup>2</sup> )	Stiffness of Coil Springs (kN/mm)	Pre-Tightening Force of FD (kN)
1	D-SCFD-1	500.00	60.00	20.00	22.16	17.99	10.00	576.69	1.17	77.95
2	D-SCFD-2	500.00	60.00	20.00	33.07	21.24	30.00	535.61	1.09	108.00
3	D-SCFD-3	500.00	60.00	20.00	43.98	24.07	50.00	499.95	1.02	134.10

To simulate the D-SCFD, the three elements of linear, multi-linear elastic, and plastic (wen) in SAP2000 were connected in parallel. The axial mechanical behavior of D-SCFD was described in the numerical model. The results from the mechanical test of D-SCFD were used to validate the method of simulation above. The parameters and hysteretic curves for validation are presented in Table 8 and Figure 18, respectively. The difference in hysteretic curves between the SAP2000 model and the test is small.

Table 8. Parameters for validation.

ID of Damper	Coil Springs		FD			SMA					
	Linear	Plastic (Wen)			Multi-Linear Elastic			Plastic (Wen)			
	$k$ (kN/mm)	$k_1$ (kN/mm)	$F_y$ (kN)	$k_2/k_1$ (%)	$u_1$ (mm)	$F_1$ (kN)	$u_2$ (mm)	$F_2$ (kN)	$k_1$ (kN/mm)	$F_y$ (kN)	$k_2/k_1$ (%)
D-SCFD	0.29	7.00	7.00	0.00	5.46	7.77	21.00	11.68	3.64	3.64	0.00

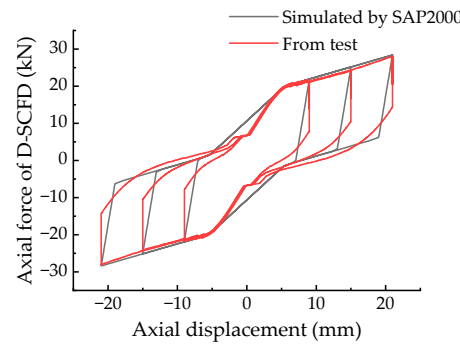


Figure 18. Comparison of hysteretic curves between the SAP2000 model and the test.

According to Table 7, the simulation parameters are presented in Table 9, which were derived from the SMA phase transition stress and strain from the test. The hysteretic curves simulated by SAP2000 are shown in Figure 19a. The simulation results of  $\xi_{eq}$  and  $R_{dr}$  had small deviations from the theoretical values, and the maximum absolute errors were only 12.14% and 1.20%, respectively. The connection between the D-SCFD and the SF is shown in Figure 19b. Compared with D-SCFD-1, the maximum SMAs' axial force of D-SCFD-2 and D-SCFD-3 decreased by 7.12% and 13.31%, respectively, which is advantageous to reduce the consumption of SMA.

Table 9. Simulation parameters of D-SCFD.

ID of Damper	Coil Springs		FD			SMA					
	Linear	Plastic (Wen)			Multi-Linear Elastic			Plastic (Wen)			
	$k$ (kN/mm)	$k_1$ (kN/mm)	$F_y$ (kN)	$k_2/k_1$ (%)	$u_1$ (mm)	$F_1$ (kN)	$u_2$ (mm)	$F_2$ (kN)	$k_1$ (kN/mm)	$F_y$ (kN)	$k_2/k_1$ (%)
D-SCFD-1	1.17	77.95	77.95	0.00	15.67	176.19	60.00	265.98	5.47	85.72	0.00
D-SCFD-2	1.09	108.00	108.00	0.00	15.67	163.51	60.00	246.91	5.09	79.74	0.00
D-SCFD-3	1.02	134.10	134.10	0.00	15.67	152.75	60.00	230.59	4.74	74.31	0.00

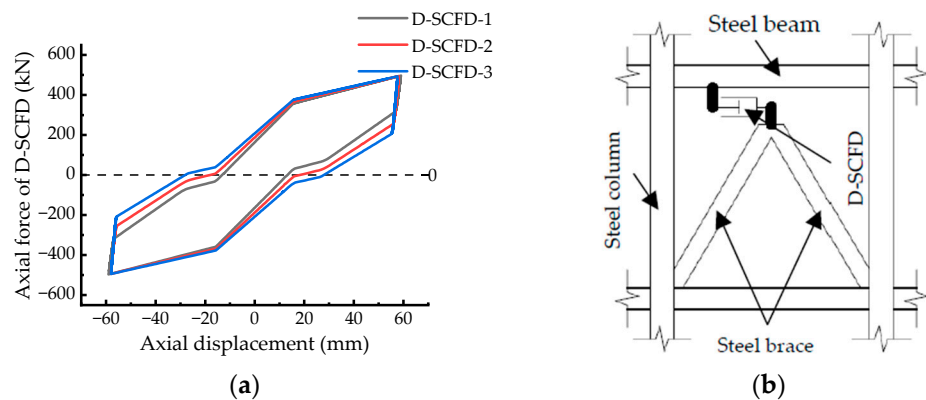
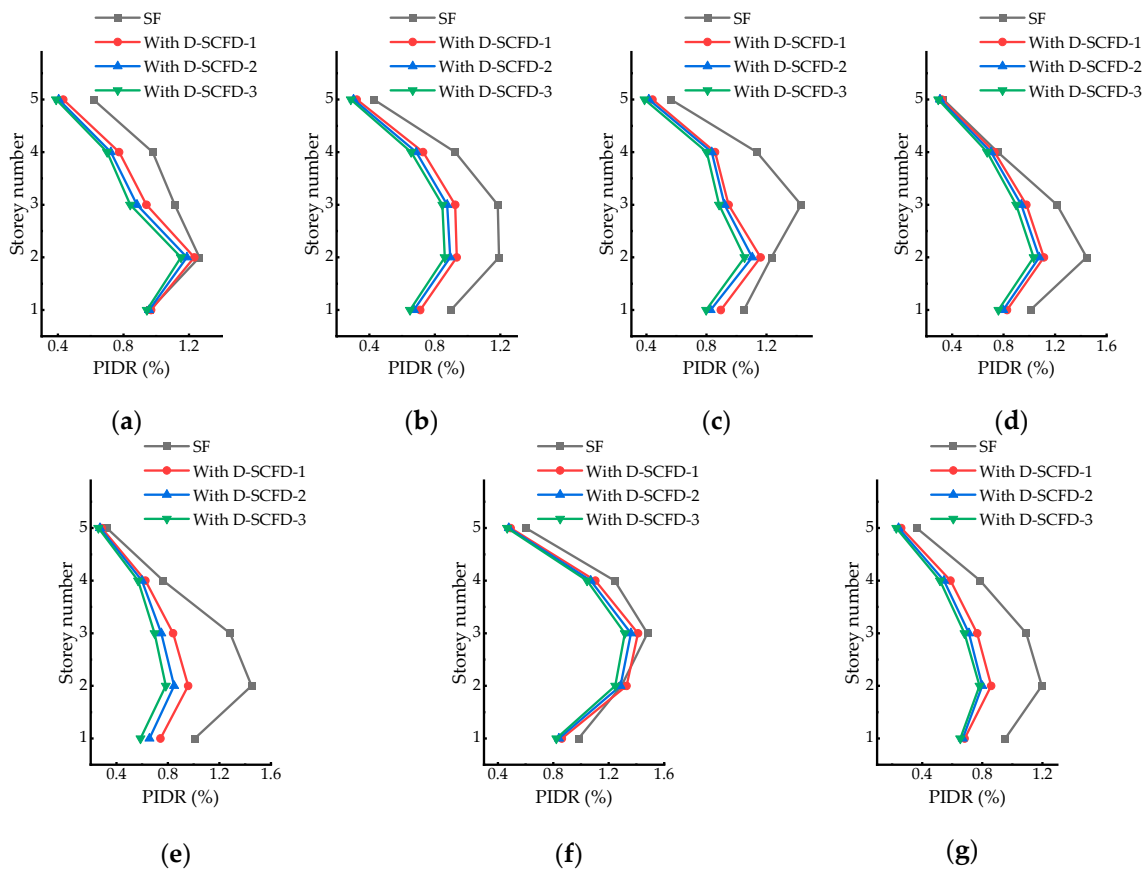


Figure 19. (a) Simulated hysteretic curves of D-SCFDs and (b) connection between D-SCFD and SF.

### 5.4. Mitigation of Seismic Responses

After the nonlinear time history analysis utilizing SAP2000, the peak inter-story drift ratios (PIDRs) under each ground motion are shown in Figure 20. D-SCFDs reduced the PIDRs of SF under the earthquake, whose safety was effectively improved. With different D-SCFDs, the maximum inter-story drifts of SF were 43.60 mm, 51.69 mm, and 50.02 mm, respectively, less than the limit of deformations. The average peak inter-story drift ratios (APIDRs) and the control rates of those under seven ground motions are shown in Table 10. Wherein, the APIDRs of the second and third floors were larger than the others. For the control effects of APIDRs, the D-SCFD-3 was better than D-SCFD-2, and the D-SCFD-2 was better than D-SCFD-1. The control impacts of APIDRs revealed that lowering the recentering performance of D-SCFDs was advantageous for improving the control effect of the structure's maximum lateral deformations, while  $R_{dr}$  did not surpass 50%.



**Figure 20.** PIDRs of structure under different ground motions: (a) GM1, (b) GM2, (c) GM3, (d) GM4, (e) GM5, (f) GM6, and (g) GM7.

**Table 10.** APIDRs and the corresponding control rates.

Number of Story	SF	SF with D-SCFD-1		SF with D-SCFD-2		SF with D-SCFD-3	
	APIDR (%)	APIDR (%)	Control Rate of APIDR (%)	APIDR (%)	Control Rate of APIDR (%)	APIDR (%)	Control Rate of APIDR (%)
1	0.980	0.813	17.04	0.775	20.92	0.774	21.02
2	1.296	1.084	16.36	1.028	20.68	0.987	23.84
3	1.257	0.973	22.59	0.919	26.89	0.881	29.91
4	0.941	0.773	17.85	0.737	21.68	0.709	24.65
5	0.461	0.365	20.82	0.347	24.73	0.330	28.42

The average residual inter-story drift ratios (ARIDRs) of the SF are shown in Table 11. D-SCFDs significantly reduced the ARIDRs of SF, which could reduce the post-seismic recovery costs of the structure. The differences in the control effects of ARIDRs were tiny, which were generated by the discrepancies in the recentering performances of D-SCFDs. The maximum difference was only 0.008%, and its level was micro. Therefore, when the  $R_{dr}$  was less than 50%, the objectives of recentering performances of D-SCFDs hardly had obvious effects on the residual deformations of the structure after an earthquake. The average peak floor accelerations (APFAs) under seven ground motions are shown in Table 12. D-SCFDs reduced the floor acceleration responses, thereby reducing the inertial forces caused by the earthquakes. Meanwhile, D-SCFD-3 had the best control effect on APFAs, followed by D-SCFD-2, and the control effect of D-SCFD-1 was relatively minimal. Differences in APFA mitigation resulted in previous variations in APIDR control rates, both of which were primarily caused by the different recentering performances of D-SCFDs. After minimizing the aims of recentering performances, the D-SCFDs had a larger value of  $\zeta_{eq}$ , which had better energy consumption performance and resulted in better APIDR and APFA mitigation.

**Table 11.** ARIDRs and the corresponding control rates.

Number of Story	SF	SF with D-SCFD-1		SF with D-SCFD-2		SF with D-SCFD-3	
	ARIDR (%)	ARIDR (%)	Control Rate of ARIDR (%)	ARIDR (%)	Control Rate of ARIDR (%)	ARIDR (%)	Control Rate of ARIDR (%)
1	0.027	0.013	51.85	0.010	62.96	0.009	66.67
2	0.054	0.025	53.70	0.020	62.96	0.017	68.52
3	0.048	0.021	56.25	0.017	64.58	0.017	64.58
4	0.021	0.012	42.86	0.010	52.38	0.009	57.14
5	0.005	0.004	20.00	0.004	20.00	0.006	−20.00

**Table 12.** APFAs and corresponding control rates.

Number of Story	SF	SF with D-SCFD-1		SF with D-SCFD-2		SF with D-SCFD-3	
	APFA (m/s <sup>2</sup> )	APFA (m/s <sup>2</sup> )	Control Rates of APFA (%)	APFA (m/s <sup>2</sup> )	Control Rates of APFA (%)	APFA (m/s <sup>2</sup> )	Control Rates of APFA (%)
1	12.03	10.31	14.30	10.03	16.63	9.82	18.37
2	14.28	11.40	20.17	10.85	24.02	10.59	25.84
3	12.35	11.87	3.89	11.37	7.94	10.94	11.42
4	15.86	14.39	9.27	13.88	12.48	13.58	14.38
5	24.09	19.52	18.97	18.71	22.33	18.01	25.24

## 6. Conclusions

In this study, a new dual self-centering damper (D-SCFD) was proposed, which was generated by connecting coil springs, SMA rods, and a friction energy dissipation device (FD) in parallel. While carrying out the mechanical tests of small-scale specimens, a simplified mechanical model was established. The theoretical index calculations of the performance of recentering and energy dissipation were derived and used to analyze the influence of coil springs, SMA rods, and FD on the performance of D-SCFD. Eventually, the seismic response control effects of D-SCFD on multi-story steel frames (SFs) were analyzed, which experienced consecutive strong earthquakes. The main conclusions are as follows:

1. The recentering and energy dissipation performances of D-SCFD were contradictory. It is necessary to define the reasonable relationship between the axial force provided by coil springs, SMA, and FD, which can make the D-SCFD give play to the ideal performance of recentering and energy dissipation.

2. After magnifying the axial force response of FD, the energy dissipation performance of D-SCFD increased, but the recentering performance decreased. Meanwhile, a reduction in the recentering performance was positively correlated with the loading displacement amplitude. After the martensitic transformation of SMA, the loading displacement amplitude had little effect on the energy dissipation performance of D-SCFD.
3. The simplified mechanical model of D-SCFD, the theoretical index calculations of the performance of recentering, and energy dissipation could accurately describe the mechanical behaviors of D-SCFD. In the suggested model, the parameters are related to the mechanical properties of each component, which is beneficial to its serviceability. With the reduction in the recentering performance target and the increase in the axial force ratio of the coil springs, the decrease in the energy dissipation performance of D-SCFD would be slower.
4. When the recentering performance of D-SCFD is required to be high, it is not appropriate to excessively increase the axial force ratio of the coil springs to avoid a rapid decline in the performance of energy dissipation. With the decrease in the recentering performance target, the proportion of axial force provided by the coil springs can be appropriately increased, thereby reducing the consumption of SMA.
5. The simulations of D-SCFD utilizing SAP2000 were close to the test. Adjusting the  $R_{dr}$  to 50% from 10%, the section area of SMA decreased by 13.31% in D-SCFD with a  $\alpha$  of 20%. Simultaneously, the control rate of the average peak inter-story drift ratio (API DR) increased 7.48% in the story with the maximum API DR. However, the maximum variation of average residual inter-story drift ratios (ARIDRs) only reached 0.008%. Therefore, when D-SCFD is used to mitigate seismic responses, the performance of recentering can be appropriately reduced.
6. Compared to the existing self-centering damper-based SMA, the consumption of SMA in D-SCFD was less, which avoided the expensive cost. In the future, the combination of a dual self-centering pattern (D-SC) and other kinds of passive energy dissipation devices could be promising.

**Author Contributions:** Conceptualization, J.Q., X.L. and Y.B.; methodology, X.L. and Y.B.; software, X.L. and Y.B.; validation, J.Q., X.L. and Y.B.; formal analysis, W.W., Y.L. and J.P.; investigation, J.Q. and W.W.; resources, J.Q.; data curation, W.W., Y.L. and J.P.; writing—original draft preparation, X.L. and Y.B.; writing—review and editing, J.Q., X.L. and Y.B.; visualization, J.Q., J.P. and C.Z.; supervision, J.Q. and J.P.; project administration, J.Q.; funding acquisition, J.Q. All authors have read and agreed to the published version of the manuscript.

**Funding:** This research was funded by the National Natural Science Foundation of China (No. 41867069) and the Yunnan Provincial Department of Education Program (No. 2023Y0260).

**Data Availability Statement:** The data presented in this study are available from the corresponding author upon reasonable request.

**Acknowledgments:** The authors extend their appreciation to the technological support from School of Architecture and Planning, Yunnan University.

**Conflicts of Interest:** The authors declare no conflicts of interest.

## Nomenclature

SMA	Shape memory alloy
FD	Friction energy dissipation device
D-SCFD	Dual self-centering friction damper
BRB	Buckling restrained brace
MYD	Metallic yielding damper
MS-AS	Mainshock–aftershock sequence
RC	Reinforced concrete
D-SC	Dual self-centering
SF	Steel frame

$W$	Dissipated energy
$K$	Secant stiffness
$\zeta_{eq}$	Equivalent viscous damping
$R_{dr}$	Rate of residual deformation
$F_{D-SCFD}$	Axial force response of D-SCFD
$k_{CS}$	Total stiffness of the coil springs
$u$	Axial deformation of D-SCFD
$t$	Time
$P$	Pre-tightening force of FD
$\mu$	Sliding friction coefficient of FD
$\text{sgn}(x)$	Symbolic function
$F_{SMA}$	Axial force of the SMA rods
$\varepsilon(x)$	Step function
$F_{SMA}^L$	Axial force responses of SMA rods during loading
$F_{SMA}^U$	Axial force responses of SMA rods during unloading
$k_{SMA,1}$	Linear stiffness of SMA rods before martensitic transformation
$k_{SMA,2}$	Linear stiffness of SMA rods after martensitic transformation
$u_{Ms}$	Axial deformation of SMA rods at the start of martensitic transformation
$F_{Ms}$	Axial force of SMA rods at the start of martensitic transformation
$u_{Mf}$	Axial deformation of SMA rods at the end of martensitic transformation
$u_{Af}$	Axial deformation of SMA rods at the end of the reverse martensitic transformation
$F_{Af}$	Axial force of SMA rods at the end of the reverse martensitic transformation
$u_{UL}^S$	Axial deformation of SMA rods at the beginning of unloading
$F_{UL}^S$	Axial force of SMA rods at the beginning of unloading
$u'_{AS}$	Axial deformation of SMA rods at the beginning of the reverse martensitic transformation
$\alpha$	Ratio of the maximum axial force of the coil springs to that of SMA rods
$\beta$	Ratio of the maximum axial force of FD to that of SMA rods
$S_a(T_1, \zeta)$	Spectral acceleration corresponding to the first translational period of structure
PIDR	Peak inter-story drift ratio
APIDR	Average peak inter-story drift ratio
ARIDR	Average residual inter-story drift ratio
APFA	Average peak floor acceleration

## References

- Almajhali, K.Y.M. Review on passive energy dissipation devices and techniques of installation for high rise building structures. *Structures* **2023**, *51*, 1019–1029. [\[CrossRef\]](#)
- Divyah, N.; Prakash, R.; Srividhya, S.; Ajay Prakash, K. Control of vibrations in high-rise structures using base isolation technology. *Mater. Today Proc.* **2023**. [\[CrossRef\]](#)
- Ilbeigi, S.; Jahanpour, J.; Farshidianfar, A. A novel scheme for nonlinear displacement-dependent dampers. *Nonlinear Dyn.* **2012**, *70*, 421–434. [\[CrossRef\]](#)
- Hussain, H.; Kim, D.-K.; Zhao, W. Advancements and Future Prospects of Buckling Restrained Braces for Corrosive-Environments: A Comprehensive Literature Review. *Buildings* **2023**, *13*, 2156. [\[CrossRef\]](#)
- Amiri, J.V.; Navayinia, B.; Navaei, S. Evaluation of performance of eccentric braced frame with friction damper. *Struct. Eng. Mech.* **2011**, *39*, 717–732. [\[CrossRef\]](#)
- Wang, J.; Men, J.; Zhang, Q.; Fan, D.; Zhang, Z.; Huang, C.-H. Seismic performance evaluation of a novel shape-optimized composite metallic yielding damper. *Eng. Struct.* **2022**, *268*, 114714. [\[CrossRef\]](#)
- Sabelli, R.; Mahin, S.; Chang, C. Seismic demands on steel braced frame buildings with buckling-restrained braces. *Eng. Struct.* **2003**, *25*, 655–666. [\[CrossRef\]](#)
- Xu, G.; Guo, T.; Li, A.; Wang, S.; Zhang, R.; Zhu, R.; Xu, J. Review on self-centering damper for seismic resilient building structures. *Structures* **2023**, *54*, 58–77. [\[CrossRef\]](#)
- Christopoulos, C.; Tremblay, R.; Kim, H.J.; Lacerte, M. Self-centering energy dissipative bracing system for the seismic resistance of structures: Development and validation. *J. Struct. Eng.* **2008**, *134*, 96–107. [\[CrossRef\]](#)
- Erochko, J.; Christopoulos, C.; Tremblay, R.; Kim, H.-J. Shake table testing and numerical simulation of a self-centering energy dissipative braced frame. *Earthq. Eng. Struct. Dyn.* **2013**, *42*, 1617–1635. [\[CrossRef\]](#)
- Erochko, J.; Christopoulos, C.; Tremblay, R. Design and Testing of an Enhanced-Elongation Telescoping Self-Centering Energy-Dissipative Brace. *J. Struct. Eng.* **2015**, *141*, 04014163. [\[CrossRef\]](#)
- Chou, C.-C.; Chung, P.-T. Development of cross-anchored dual-core self-centering braces for seismic resistance. *J. Constr. Steel Res.* **2014**, *101*, 19–32. [\[CrossRef\]](#)

13. Chou, C.-C.; Chen, Y.-C. Development of Steel Dual-Core Self-Centering Braces: Quasi-Static Cyclic Tests and Finite Element Analyses. *Earthq. Spectra* **2015**, *31*, 247–272. [[CrossRef](#)]
14. Chou, C.-C.; Tsai, W.-J.; Chung, P.-T. Development and validation tests of a dual-core self-centering sandwiched buckling-restrained brace (SC-SBRB) for seismic resistance. *Eng. Struct.* **2016**, *121*, 30–41. [[CrossRef](#)]
15. Wang, Y.; Zhou, Z.; Ge, H.; Yao, J.; Xie, Q. Experimental validation and numerical simulation of a dual-self-centering variable friction braced frame under strong ground motions. *J. Build. Eng.* **2022**, *56*, 104761. [[CrossRef](#)]
16. Xie, Q.; Zhou, Z.; Meng, S.-P. Experimental investigation of the hysteretic performance of self-centering buckling-restrained braces with friction fuses. *Eng. Struct.* **2020**, *203*, 109865. [[CrossRef](#)]
17. Xu, L.-H.; Fan, X.-W.; Li, Z.-X. Cyclic behavior and failure mechanism of self-centering energy dissipation braces with pre-pressed combination disc springs. *Earthq. Eng. Struct. Dyn.* **2017**, *46*, 1065–1080. [[CrossRef](#)]
18. Xu, L.; Fan, X.; Li, Z. Experimental behavior and analysis of self-centering steel brace with pre-pressed disc springs. *J. Constr. Steel Res.* **2017**, *139*, 363–373. [[CrossRef](#)]
19. Fan, X.-W.; Xu, L.-H.; Li, Z.-X. Behaviors Comparisons and Prediction of Pre-Pressed Spring Self-Centering Energy Dissipation Braces. *Int. J. Struct. Stab. Dyn.* **2018**, *18*, 1840006. [[CrossRef](#)]
20. Filiatrault, A.; Tremblay, R.; Kar, R. Performance evaluation of friction spring seismic damper. *J. Struct. Eng.-ASCE* **2000**, *126*, 491–499. [[CrossRef](#)]
21. Khoo, H.-H.; Clifton, C.; Butterworth, J.; MacRae, G.; Gledhill, S.; Sidwell, G. Development of the self-centering Sliding Hinge Joint with friction ring springs. *J. Constr. Steel Res.* **2012**, *78*, 201–211. [[CrossRef](#)]
22. Khoo, H.-H.; Clifton, C.; Butterworth, J.; MacRae, G. Experimental Study of Full-Scale Self-Centering Sliding Hinge Joint Connections with Friction Ring Springs. *J. Earthq. Eng.* **2013**, *17*, 972–997. [[CrossRef](#)]
23. Dolce, M.; Cardone, D.; Marnetto, R. Implementation and testing of passive control devices based on shape memory alloys. *Earthq. Eng. Struct. Dyn.* **2000**, *29*, 945–968. [[CrossRef](#)]
24. Qian, H.; Li, H.; Song, G.; Guo, W. Recentering Shape Memory Alloy Passive Damper for Structural Vibration Control. *Math. Probl. Eng.* **2013**, *2013*, 963530. [[CrossRef](#)]
25. Shi, F.; Saygili, G.; Ozbulut, O.E. Probabilistic seismic performance evaluation of SMA-braced steel frames considering SMA brace failure. *Bull. Earthq. Eng.* **2018**, *16*, 5937–5962. [[CrossRef](#)]
26. Shi, F.; Ozbulut, O.E.; Zhou, Y. Influence of shape memory alloy brace design parameters on seismic performance of self-centering steel frame buildings. *Struct. Control Health Monit.* **2020**, *27*, e2462. [[CrossRef](#)]
27. Shi, F.; Zhou, Y.; Ozbulut, O.E.; Cao, S. Development and experimental validation of anchorage systems for shape memory alloy cables. *Eng. Struct.* **2021**, *228*, 111611. [[CrossRef](#)]
28. Shi, F.; Zhou, Y.; Ozbulut, O.E.; Ren, F. Hysteretic response and failure behavior of an SMA cable-based self-centering brace. *Struct. Control Health Monit.* **2022**, *29*, e2847. [[CrossRef](#)]
29. Rayegani, A.; Soureshjani, O.K.; Alae, S.A.M.; Mualla, I.H.; Nemati, F. Seismic Performance of Buildings Equipped with Four-Joint Rotational Friction Dampers in Mainshock–Aftershock Sequences. *J. Struct. Eng.* **2023**, *150*, 04023235. [[CrossRef](#)]
30. Li, Y.; Zhang, H.; Wang, J.; Yu, H.; Ma, K.; Zhang, X.; Ji, W.; Li, R. Experimental investigation on the seismic behavior of a novel self-centering friction damper. *J. Build. Eng.* **2023**, *76*, 107384. [[CrossRef](#)]
31. Chen, J.; Wang, W.; Fang, C. Manufacturing, testing and simulation of novel SMA-based variable friction dampers with enhanced deformability. *J. Build. Eng.* **2022**, *45*, 103513. [[CrossRef](#)]
32. Qiu, C.; Liu, J.; Du, X. Cyclic behavior of SMA slip friction damper. *Eng. Struct.* **2022**, *250*, 113407. [[CrossRef](#)]
33. Zheng, W.Z.; Tan, P.; Li, J.; Wang, H.; Liu, Y.H.; Xian, Z.B. Superelastic pendulum isolator with multi-stage variable curvature for seismic resilience enhancement of cold-regional bridges. *Eng. Struct.* **2023**, *284*, 115960. [[CrossRef](#)]
34. Zheng, W.Z.; Tan, P.; Zhang, Z.H.; Wang, H.; Sun, Z. Damping enhanced novel re-centering seismic isolator incorporating superelastic SMA for response control of bridges under near-fault earthquakes. *Smart Mater. Struct.* **2022**, *31*, 065015. [[CrossRef](#)]
35. Hussain, E.; Kalaycioglu, S.; Milliner, C.W.D.; Cakir, Z. Preconditioning the 2023 Kahramanmaraş (Turkiye) earthquake disaster. *Nat. Rev. Earth Environ.* **2023**, *4*, 287–289. [[CrossRef](#)]
36. Lu, X.; Cheng, Q.; Xu, Z.; Xiong, C. Regional seismic-damage prediction of buildings under mainshock-aftershock sequence. *Front. Eng. Manag.* **2021**, *8*, 122–134. [[CrossRef](#)]
37. Raghunandan, M.; Liel, A.B.; Luco, N. Aftershock collapse vulnerability assessment of reinforced concrete frame structures. *Earthq. Eng. Struct. Dyn.* **2015**, *44*, 419–439. [[CrossRef](#)]
38. Wen, W.; Ji, D.; Zhai, C.; Li, X.; Sun, P. Damage spectra of the mainshock-aftershock ground motions at soft soil sites. *Soil Dyn. Earthq. Eng.* **2018**, *115*, 815–825. [[CrossRef](#)]
39. Yu, X.-H.; Li, S.; Lu, D.-G.; Tao, J. Collapse Capacity of Inelastic Single-Degree-of-Freedom Systems Subjected to Mainshock-Aftershock Earthquake Sequences. *J. Earthq. Eng.* **2020**, *24*, 803–826. [[CrossRef](#)]
40. Zhou, Z.; Xu, H.; Gardoni, P.; Lu, D.; Yu, X. Probabilistic demand models and fragilities for reinforced concrete frame structures subject to mainshock-aftershock sequences. *Eng. Struct.* **2021**, *245*, 112904. [[CrossRef](#)]
41. Lagoudas, D.C.; Mayes, J.J.; Khan, M.M. Simplified shape memory alloy (SMA) material model for vibration isolation. In Proceedings of the Smart Structures and Materials 2001 Conference, Newport Beach, CA, USA, 5–8 March 2001.
42. Brinson, L.C. One-Dimensional Constitutive Behavior of Shape Memory Alloys: Thermomechanical Derivation with Non-Constant Material Functions and Redefined Martensite Internal Variable. *J. Intell. Mater. Syst. Struct.* **1993**, *4*, 229–242. [[CrossRef](#)]

43. Auricchio, F.; Taylor, R.L.; Lubliner, J. Shape-memory alloys: Macromodelling and numerical simulations of the superelastic behavior. *Comput. Methods Appl. Mech. Eng.* **1997**, *146*, 281–312. [[CrossRef](#)]
44. *GB 50011-2010*; Code for Seismic Design of Buildings. China Architecture and Building Press: Beijing, China, 2016.
45. Vamvatsikos, D.; Cornell, C.A. Direct estimation of seismic demand and capacity of multidegree-of-freedom systems through incremental dynamic analysis of single degree of freedom approximation. *J. Struct. Eng.* **2005**, *131*, 589–599. [[CrossRef](#)]

**Disclaimer/Publisher’s Note:** The statements, opinions and data contained in all publications are solely those of the individual author(s) and contributor(s) and not of MDPI and/or the editor(s). MDPI and/or the editor(s) disclaim responsibility for any injury to people or property resulting from any ideas, methods, instructions or products referred to in the content.